

1420 MHz Continuum Absorption toward Extragalactic Sources in the Galactic Plane

S. Strasser

Department of Astronomy, University of Minnesota, Minneapolis, MN 55455

A.R. Taylor

Department of Physics and Astronomy, University of Calgary, Calgary, AB T2N 1N4

strasser@astro.umn.edu, russ@ras.ucalgary.ca

ABSTRACT

We present a 21-cm emission-absorption study towards extragalactic sources in the Canadian Galactic Plane Survey (CGPS). We have analyzed H I spectra towards 437 sources with $S_\nu \geq 150$ mJy, giving us a source density of 0.6 sources per square degree at arcminute resolution. We present the results of a first analysis of the H I temperatures, densities, and feature statistics. Particular emphasis is placed on 5 features with observed spin temperatures below 40 K.

We find most spin temperatures in the range from 40 K to 300 K. A simple H I two-component model constrains the bulk of the cold component to temperatures (T_c) between 40 K and 100 K. T_c peaks in the Perseus arm region and clearly drops off with Galactocentric radius, R , beyond that. The H I density follows this trend, ranging from a local value of 0.4 cm^{-3} to less than 0.1 cm^{-3} at $R = 20$ kpc. We find that H I emission alone on average traces about 75% of the total H I column density, as compared to the total inferred by the emission and absorption. Comparing the neutral hydrogen absorption to CO emission no correlation is found in general, but all strong CO emission is accompanied by a visible H I spectral feature. Finally, the number of spectral H I absorption features per kpc drop off exponentially with increasing R .

Subject headings: Galaxy: disk—Galaxy: fundamental parameters—ISM: atoms—radio lines: ISM

1. INTRODUCTION

In the last 30 years our knowledge of the interstellar neutral hydrogen (H I) in the Galaxy has expanded dramatically. Many of the discoveries came from emission-absorption

studies towards continuum background sources at 1420 MHz. Perhaps the most important realization of the early surveys (e.g. Clark 1965; Hughes et al. 1971; Radhakrishnan et al. 1972) was that the emission line-widths are clearly broader than the corresponding absorption, indicating that the emitting gas must be dominated by a much warmer phase than the absorbing gas. Lazareff (1975), Dickey et al. (1978), Mebold et al. (1982) analyzed the spin temperature (T_s), and found values from approximately 40 K up to several thousand Kelvin, peaking between 80 K and 150 K. Due to the probable mix of cold and warm gas, the physical interpretation of T_s has remained difficult. Braun and Walterbros (1992) applied a two-component model to absorption and emission data and found cold phase temperatures in agreement with the above spin temperatures. However two recent studies (Heiles and Troland 2003a,b; Dickey 2002), fitting individual features, find the cold component temperature peaking between 40 K and 60 K. Heiles and Troland (2003b) also finds the warm component ranging from roughly 1000 K to 9000 K. This puts ideas about the ISM existing in distinct stable temperature and density regimes (e.g. McKee and Ostriker 1977) into question. We also do not have a firm theoretical or observational basis on the lower limit (if such exists) of the cold component temperature, before most of the gas becomes molecular.

Addressing the variation with Galactocentric radius, Kulkarni and Heiles (1988) state that the supernova-dominated McKee-Ostriker (MO) model (McKee and Ostriker 1977) might describe the inner Galaxy better, while the outer, more quiescent, Galaxy is better described by the FGH model (Field et al. 1969). Dickey et al. (2003) and Kolpak et al. (2002) define the mean opacity, $\langle \kappa \rangle$, as the optical depth line of the sight integral divided by the radial velocity change due to the rotation curve, for radial increments in the Galaxy. They found an decrease in $\langle \kappa \rangle$ with increasing radius in the first and fourth quadrant respectively. Overall, however, our knowledge of the radial variation of the ISM phases is still quite limited. This is mainly because of the time requirements to observe a large number of sources over a wide area of the Galactic plane at the sensitivity needed to get a good source density. New surveys, as those used by Dickey et al. (2003) and Kolpak et al. (2002), are starting to give us a much better picture of the H I states and the variations with Galactocentric radius.

We present a new emission-absorption study toward compact continuum background sources in the Canadian Galactic Plane Survey (CGPS, Taylor et al. 2003). We have applied an “on-off method” to extract the emission brightness temperature and optical depth toward the sources. Due to the high resolution and sensitivity of the CGPS we are able to study the radial variation of the H I temperature and density for a much higher source density in the Galactic Plane than ever before. Section 2 gives an overview of the CGPS and the on-off method used. In section 3 we present the spin temperatures and the results of a simple two-temperature model. Further we discuss the spatial variation of the H I column density,

and the correlation with CO. We also present a brief analysis of absorption feature statistics. Section 4 summarizes our results and indicates some areas of future research.

2. OBSERVATIONS AND THE ON-OFF METHOD

2.1. The CGPS 21-cm dataset

The Canadian Galactic Plane Survey (Taylor et al. 2003) is a multi-wavelength study at 1 arc-minute resolution from Galactic longitude 74° to 147° , and latitude -3.6° to 5.6° . The observations for the 21 cm dataset were carried out with the Dominion Radio Astrophysical Observatory (DRAO) Synthesis Array, near Penticton, Canada (for a description, see Landecker et al. 2000). The array consists of seven 9-metre antennas. Four of the antennas are movable to yield a total of 12 configurations, or 144 baselines. For the survey each field was observed in each position for 12 hours to obtain full uv-sampling. Short spacing data were taken with the DRAO 26-m single dish telescope. At 21-cm the CGPS images have a spatial resolution of $1' \times 1' \text{cosec}(\delta)$. The instrumental velocity resolution of 1.319 km/s is sampled every 0.824 km/s, covering LSR velocities from approximately 40 km/s to -160 km/s. The RMS noise of the emission in a single velocity channel at the field centres is about 3 K in low emission regions, and up to 6 K in high emission regions (Gibson et al. 2000). The continuum data are taken in four 7.5 MHz bands (centred on 1406.9 MHz, 1413.8 MHz, 1427.4 MHz, and 1434.3 MHz). A technical matter of importance for our work is the fact that a slightly different uv-taper is applied to the (continuum subtracted) H I datacube than the continuum maps. We convolved the CGPS continuum maps to match the beam shapes exactly. For a detailed description of the data acquisition and reduction process see Taylor et al. (2003).

2.2. Compact Continuum Background Sources in the CGPS

For this study we have identified 437 compact sources with a peak continuum brightness temperature higher than 30 K in the CGPS, corresponding to integrated flux densities higher than 150 mJy. The cut-off value of 30 K was chosen because the absorption signal to noise for sources below this temperature is almost always less than 1. This gives a source density of about 0.6 sources per square degree in the CGPS area. Figure 1 shows the source locations. The sources provide a fairly uniform coverage of this section of the Galactic plane. Note that we do not exclude any sources that might be of Galactic origin. By inspecting the emission versus absorption velocity cut-offs we find about 15 potential Galactic sources.

2.3. The On-Off Method

Past emission-absorption studies typically used one on-source position and several off-source positions distributed around the source to approximate the "unabsorbed" spectrum (e.g. a hexagonal pattern, see Colgan et al. (1988)). For this work a different approach was taken, since we have a fully sampled, mosaiced dataset. First, the continuum sources were fitted with 2-D elliptical Gaussians. An average off-source emission brightness temperature, $T_B(v)$, was then extracted in a one arc-minute wide elliptical annulus, with its inner edge tracing the fitted ellipse in shape but scaled to be one FWHM from the centre. Most sources are unresolved, so the annuli are typically approximately one arc-minute (one beamwidth) away from the source centre. The RMS variations in $T_B(v)$ over the annulus give an estimate of the emission error. The off temperature is assumed to represent the emission on-source in the absence of continuum absorption. It is thus important to keep the separation between the on and off measurement directions as small as possible. At 1 kpc line of sight distance, one arc-minute corresponds to about 0.3 pc.

An average optical depth (τ) was computed from the on-source spectrum using pixel values within one HWHM from the centre of the background source, and any pixels further away for which the emission temperature signal to noise was higher than 5. Under Local Thermal Equilibrium (LTE) the optical depth in any channel is then given by

$$\exp[-\tau(v)] = \left\langle 1 - \frac{T_B - T_{on}(x, y)}{T_{bg}(x, y)} \right\rangle \quad (1)$$

where T_{bg} is the continuum brightness temperature of the background source and $T_{on}(x, y)$ is the continuum subtracted profile at the pixel location (x, y) . Typically about 10 pixels per channel are used in the average optical depth computation. The spin temperature is derived by,

$$T_s(v) = \frac{T_B(v)}{1 - e^{-\tau(v)}} \quad (2)$$

Note that for large optical depth, $T_B - T_{on}$ approaches T_{bg} . Due to noise in the data the optical depth can diverge. This situation was typically encountered for at least a few channels in any given spectrum. Since this corresponds to completely optically thick gas, we set $\exp(-\tau)$ and $T_s(v)$ equal to zero and $T_B(v)$ respectively in these cases.

To test our on-off method we inserted absorption from artificial background sources into the data cubes. The artificial continuum sources were Gaussian shaped to match the synthesized beam and had peak brightness temperatures ranging from 30 K to 300 K. The line emission brightness temperature in each channel was modified at the position of the artificial source in proportion to the background source intensity and the H I brightness in that channel at the source position. The resulting absorption spectra were extracted using

the on-off method and compared to the known input profiles. The agreement between the two was consistently well within one sigma for both the spin temperatures and optical depth spectra. We also compared spectra common to this study and Dickey et al. (1983). In general the agreement is good, but in noisy channels they sometimes differ by several σ .

3. RESULTS AND INTERPRETATION

Figures 2 and 3 show two representative spectra, illustrating the quality of the data for two sources with very different continuum brightness temperatures. We do not show all the spectra in this paper due to their large number. All the spectral data are available online (<http://www.ras.ualgary.ca/CGPS/products/>) or by request from S. Strasser. Some features are common to many spectra. We can almost always identify the local (10 to -20 km/s) and Perseus arms (around -25 to -50 km/s) as broad peaks in emission, and in many cases also the outer arm (between -80 and -110 km/s). In general the absorption spectra show more structure and narrower line widths than the emission spectra. However this difference is less pronounced than for past, lower angular resolution, studies. Some features follow the “ $T_s - \tau$ relation” ($\log \tau$ decreases linearly with increasing $\log T_s$) quite nicely. This is attributed to the difference in absorption versus emission line widths, as the former is dominated by cool gas, and the latter by the warm component. In many cases however, the observed relation is more in the shape of a loop, where the spin temperature for a given optical depth on one side of the feature is systematically higher or lower than on the other side. Several recent studies confirm this relationship (see e.g. Dickey et al. 2003).

3.1. The Spin Temperatures

The spin temperature (T_s) is the simplest temperature indicator we can compute. Under assumption of a single-component medium in equilibrium it is equal to the kinetic temperature of the gas (e.g. Kulkarni and Heiles 1988). The distribution of spin temperatures is given in figure 4 for all channels with $S/N(T_{on-off}) > 5$ (6318 channels in total). The median of the distribution is 120 K, and 90% of the values lie between 60 K and about 280 K. This is in rough agreement with previous studies (Dickey et al. 1978; Mebold et al. 1982; Payne et al. 1982) and recent results for the southern Galactic plane (Dickey et al. 2003).

It is generally believed though that the neutral hydrogen has at least two components, the cold neutral medium (CNM) and the warm neutral medium (WNM). The spin temperature measures a harmonic mean of the CNM and WNM, weighted by the column density of

each component. It therefore only provides us with an upper limit to the true cold component temperature and a lower limit to the warm component temperature. This is confirmed by more recent analyses that fit the CNM and WNM separately and find lower cold component H I temperatures than the associated spin temperatures. By fitting profiles with Gaussian functions Heiles and Troland (2003a,b) find cold component temperatures in the range from about 10 K to 75 K. Dickey et al. (2003) use a novel technique of fitting the emission and absorption and find a range for the cold temperature between 20 K and 110 K, much lower than their spin temperatures.

3.2. A 2-Component Model

We have applied a two-component model to the data extracted from the CGPS. Our approach is similar to a model applied to the Galaxy and M31 by Braun and Walterbros (1992). We use the transfer equation for a case where two components contribute to the emission brightness temperature:

$$T_B(v) = T_w (1 - e^{-\tau_w(v)q}) + T_c (1 - e^{-\tau_c(v)}) e^{-\tau_w(v)q} + T_w (1 - e^{-\tau_w(v)(1-q)}) e^{-[\tau_c(v)+\tau_w(v)q]} \quad (3)$$

Here we assume that the gas has a cold component at temperature T_c and optical depth $\tau_c(v)$ and a warm component at temperature T_w with optical depth $\tau_w(v)$. A fraction q of the warm gas is in front of the cold gas at every velocity. The first term in equation 3 represents WNM emission in front of the CNM. The second term accounts for the CNM emission, absorbed by the WNM in front. The third term represents the WNM behind the cold component, which is absorbed by both the CNM and WNM foregrounds. Since $\tau \propto N/T$, we further assume that the absorption due to the WNM is much smaller than that due to the CNM and that the WNM does not absorb the CNM. For $\tau_w(v) \ll \tau_c(v)$ and $\tau_w(v) \ll 1$ we then derive

$$T_B(v) = T_0(v)e^{-\tau_c(v)} + T_\infty(v) (1 - e^{-\tau_c(v)}) \quad (4)$$

where $T_0 = T_w\tau_w(v)$ and $T_\infty = T_w\tau_w(v)q + T_c$ are the limits of T_B as τ_c goes to zero and infinity respectively. Note that, even though these limiting temperatures are functions of velocity, we treat them as constants by assuming that $\tau_w(v)$ is approximately constant. We make this assumption because we fit the data for all sources at once, hence averaging out the velocity dependence.

In figure 5 a scatter plot of $T_B(v)$ versus $1 - e^{-\tau_c(v)}$ for all sources is displayed. On these axes T_0 and T_∞ are the values of the $T_B(v)$ at $1 - e^{-\tau_c(v)}$ equal to 0 and 1 respectively. Every data point represents one velocity channel. Only points with T_{on-off} S/N higher than 5 are plotted. The centre line is a least squares fit of equation 4 to the data, yielding T_0

= 24 K and $T_\infty = 88$ K. We cannot explicitly solve for T_w , only the factor $T_\infty = T_w\tau_w$. Statistically, however, we expect an average value of $q = 0.5$, and assuming this we can solve for the cold component temperature. This gives $T_c = 76$ K. Varying q gives an estimate of the uncertainty in the average cold component temperature. T_c goes to 88 K and 64 K for q equal to 0 and 1 respectively.

We interpret the scatter in the fit as being due to a range of T_c and $T_0 = T_w\tau_w$. In figure 5 we show visually selected upper and lower envelopes with the form of equation 4 (solid lines). T_0 ranges from 0 K to 60 K. Points on the lower envelope, which has $T_0 = 0$, thus represent regions where there is no warm component, and as we move toward the upper envelope, T_c and T_∞ increase. From the envelopes we find T_c ranging between 50 K and 100 ± 30 K (the upper limit is for $q = 0.5$ and the uncertainty comes from varying q between 0 and 1).

There are a few scattered points below the lower envelope. We analyzed these points in more detail to see if they could be due to a very cold neutral hydrogen component (below 40 K). We find that several well defined (relatively unblended) features contribute most of the points. Table 1 summarizes these features. Selecting features with line centre T_s below 40 K yields the same list. The optical depth and spin temperature line profiles for these features are shown in figure 6. The last column in table 1 shows the cold temperatures obtained by fitting our two-component model to each feature region individually (for a $q = 0.5$). Fitting individual features in this way is similar to the approach taken by Dickey et al. (2000), except that we fit two components instead of one, and the fitting is done by least squares rather than by eye. The cold temperatures are confirmed by the two-component model. Except for the feature towards (85.089, +3.620), which has a computed T_c of only 4 K (range of 0 K for $q = 1$ to 13 K for $q = 0$), all of the features have a T_c of approximately 20 K, with a typical range between 10 K for $q = 1$ and 30 K for $q = 0$. Note that the velocities of these features place all of them quite far in the outer Galaxy (unfortunately making it unlikely that they show up as H I self-absorption).

While the model envelopes (figure 5) fit the data reasonably well, we can clearly see that T_{off} increases more rapidly at small τ_c and flattens out at a maximum value of approximately 120 K. This peak brightness temperature is a well known observational fact for spiral galaxies. We are probably seeing two effects here: First, because galactic rotation spreads out the gas in velocity, only a certain amount of gas ever piles up at the same velocity limiting the maximum brightness temperature (Dickey et al. 2003). Second, clearly if the optical depth in a line becomes much greater than 1, it will start to saturate, which creates a non-linear dependence of T_B on $e^{-\tau}$. These two effects would explain why a simple radiation transfer, as modeled, does not fit the upper envelope better. The dashed line in figure 5 shows a fit

to the upper envelope below the “break” with $T_0 = 25$ K and $T_\infty = 212$ K. For $q = 0.5$ this gives a cold component temperature, $T_c = 200$ K (with a range from 188 K to 212 K for q equal to 1 and 0 respectively). If saturation is a dominant effect at high optical depth, then this line reflects what the state of the unsaturated gas is. The much higher T_c value obtained by this fit, compared to fitting the whole range of τ , is accounted for by the fact that the warmer the gas gets, the harder it is for it to reach high optical depth.

Braun and Walterbros (1992), applied a similar model to data for 87 sources covering a large range of Galactic latitude. They found best fit values of $T_c = 105$ K and $T_0 = 4$ K, and envelope values from 54 K to 157 K for T_c and from 2 K to 6 K for T_0 . The inconsistency between these and our results might arise primarily from the typically higher latitude of sources used in their study.

3.3. Radial Variation of Physical Conditions

3.3.1. Temperature

We examined the radial variation of the temperature by fitting the two-component model to bins in Galactocentric radius. We used the rotation curve from Brand and Blitz (1993) to compute the Galactocentric radius corresponding to a given velocity, assuming a rotation velocity of 220 km/s for the local standard of rest, and 8.5 kpc Galactic centre to Sun distance. To find the radial variation of our model parameters, T_c and T_0 , we binned the data in 1 kpc intervals out to 16 kpc and beyond in 2 kpc intervals to 20 kpc. The bin sizes were chosen so that every bin contains a large enough number of points to apply our model. We fitted the data for each bin in the same way as the whole dataset in section 3.2, finding a best fit value and an upper and lower envelope.

Figure 7 shows the variation of T_c and T_0 as a function of radius for $q = 0.5$. The dots show the fitted values, while the lines above and below indicate the temperature range given by the envelopes. The average cold component temperature rises from a local value of about 65 K to 80 K around 14 kpc and then drops off to 45 K in the outer Galaxy. The uncertainty introduced by q is a maximum of about 20 K for the inner bins, and drops to around 10 K in the outer bins ($R > 14$ kpc). The lower envelope follows the same trend ranging from 40 K to 60 K, while the upper envelope depends only weakly on R ranging from 80 K to 100 K, with a minimum around 12 kpc and a peak at 14 kpc.

T_0 starts out at a maximum value of 36 K, and also has a local peak around 14 kpc before falling off to about 10 K at 20 kpc. These results indicate that warm gas is rare in the outer Galaxy. Of course the variation in T_0 could be due to a combination of changing

warm temperature and opacity. Further, at 20 kpc a line of sight at latitude 5° is 1.8 kpc above the plane, and the Galactic warp could be as large as 4 kpc (Dickey and Lockman 1990). Especially the negative latitude lines of sight can thus look at quite a different height of the disk locally as compared to the far outer Galaxy. This could affect our results (our spin temperatures, however, do not indicate any dependence on z).

3.3.2. Volume Densities

We have used the absorption and emission spectra to study the density of the H I gas. For a gas at temperature $T_s = T_B(1 - e^{-\tau})$ the element of column density in a velocity channel of width Δv is given by

$$\Delta N(v) = \frac{C\tau(v)T_B(v)}{1 - e^{-\tau}}\Delta v \quad (5)$$

and represents the number of atoms per cm^2 in the velocity range v to $v + \Delta v$. For v in km/s, the constant C is equal to $1.83 \times 10^{18} \text{ cm}^{-2}\text{K}^{-1}(\text{km/s})^{-1}$. A spatial density as a function of Galactocentric radius can be computed by dividing the line of sight into R bins. The density, $n(R)$ in any bin is given by,

$$n(R) = \frac{\sum_{\Delta V} N(v)}{\Delta L} \quad (6)$$

where ΔL is the line of sight distance through the bin and ΔV is the corresponding velocity range computed from Brand and Blitz (1993). Figure 8 shows the mean density as a function of Galactocentric radius for all the sources. A robust exponential least-squares fit of the form $y = Ae^{-Bx}$ to the distribution is shown, which characterizes the decrease quite well beyond 14 kpc, with values for $A = 6.04 \text{ cm}^{-3}$ and $B = 0.29 \text{ kpc}^{-1}$. We can see a local increase in the density around 12 kpc, due to the Perseus arm.

We also examine the variation of density with height above the plane, z . To derive a spatial density as a function of z , $n(z)$, we sum the data in a given z bin as in equation 6, but now ΔV refers to the velocity range contributing to the bin and ΔL is the line of sight range, as before. In figure 9 we show the mean value of $n(v)$ as a function of z . The mean of the density drops off with scale heights of approximately 350 and 280 pc above and below the plane respectively (found from exponential fits to the positive and negative sides of the distribution). The difference is due to the Galactic warp, which shows up as a density enhancement clearly visible at positive z in figure 9. The scale heights correspond to a combination of the warm and cold components (averaged over the CGPS region).

In the absence of information on absorption, H I mass is often inferred from emission line data. The question of the ability to trace H I gas by the emission alone is thus interesting

to address. In deriving H I mass from emission the optically-thin case is assumed where equation 5 reduces to

$$N_{em}(v) = CT_B(v)\Delta v, \quad (7)$$

where we have designated N_{em} as the column density derived from emission alone. Figure 10 shows the emission column density, N_{em} , versus the column density N_{HI} given by absorption using equation 5. By combining equation 5 with equation 7 we can find a functional relation between N_{HI} and N_{em} ,

$$N_{HI} = -A \ln \left(1 - \frac{N_{em}}{A} \right) \quad (8)$$

where $A = CT_s\Delta v$. In reality many different spin temperatures contribute to each measured column density. However equation 8 provides a convenient way to characterize the relationship between N_{HI} and N_{em} . By least squares fitting the parameter A, we find a value of $2.1 \times 10^{22} \text{ cm}^{-2}$; The corresponding fit is shown in figure 10 and well represents the data.

The average ratio of N_{HI}/N_{em} is equal to 1.32 (or $N_{em} = 75\%$ of N_{HI}). At the highest column densities N_{em} measures only about 65% of the true column. Dickey et al. (2003) find typical values for N_{HI}/N_{em} of 1.4 to 1.6 in the inner Galaxy. Dickey et al. (1983) derived a somewhat lower value of 1.2 for N_{HI}/N_{em} . The difference is probably due to our concentration of lines of sight very close to the Galactic plane, where the opacity is highest, so the difference between N_{HI} and N_{em} is the largest on average. Heiles and Troland (2003a) clearly show this dependence of N_{HI}/N_{em} on Galactic latitude in their figure 5, and their values close to the Galactic plane qualitatively agree with the results presented here.

3.4. Correlation with CO

Another of the CGPS data products are the reprocessed images from the FCRAO Outer Galaxy Survey of the $^{12}\text{CO J} = 1 - 0$ rotational transition at 2.6 mm (Heyer et al. 1998). The survey has an angular resolution of 1.67 arc-minutes, and covers the same velocity range as the 21-cm dataset at the same spectral resolution. CO is often used as a tracer for molecular hydrogen, as it exists in a similar physical environment. The accuracy with which it traces H_2 , however, is still a subject of frequent debate. While the presence of CO correlates with H_2 or very cold atomic hydrogen, the reverse often does not seem to be the case (e.g Reach et al. 1994; Meyerdierks and Heithausen 1996).

Recent studies (Gibson et al. 2000; Heiles and Troland 2003b; Knee and Brunt 2001; Kavars and Dickey 2003) are finding clear evidence for H I below 30 K, where we expect most the hydrogen to be in molecular form. Our own 2-component analysis reveals several absorption features below 40 K. To check for the co-existence of H I absorbing gas and

molecular material we compared the H I absorption spectra to the CO emission spectra towards the sources.

Figure 11 shows the CO emission brightness temperature versus the H I optical depth for the 134 sources which are in the FCRAO survey area (from Galactic longitude 102° to 143° and all CGPS latitudes). It is evident that overall there is no correlation between the CO emission and H I absorption. The CO noise level is ~ 0.15 K. There is a very clear lack of data points with CO emission brightness temperature above the noise level at low H I optical depth. This, and visual inspection of the spectra, show that in most cases where we do see CO emission, H I absorption is also present. We find about 60 clear matches between H I and CO features, and for approximately 20 of these, $e^{-\tau}$ goes to zero. Many such features are only a few channels wide both in CO and H I optical depth. Figure 12 shows two sample features. The narrow feature in the left panel, illustrates a case in which $e^{-\tau}$ goes to zero. The panel on the right displays two broad H I absorption lines, one of which shows a clear correlation with CO emission.

Of the two cold features listed in table 1 for which we have CO data, one (112.107,+2.362) has associated CO emission. In general, however, there is no preference for low spin temperatures in H I channels with associated CO. As noted earlier though, if a cloud has multiple temperature components, the spin temperature is a harmonic mean, and therefore, even if the cold-component temperature is very low, the apparent spin temperature does not necessarily have to be low. So, while there is no overall correspondence between the CO and H I features, the association of over 60 features is interesting, and a good indication that at least some of the atomic hydrogen is at very low temperatures. We plan to pursue this by modeling the individual features and by obtaining more observations at higher spectral resolution and signal to noise to be able to better quantify our current results.

3.5. Feature Distribution and Properties

The spatial density of absorption peaks is a simple tracer of cold ISM structures. An absorption feature in general corresponds to one cloud, or more if several lines are blended. The feature density (number of features per kpc) is thus a lower limit to the cloud density. We have developed an automatic absorption feature identification routine that finds peaks in the T_{on-off} spectra. Such an identification is never completely unambiguous, as noise spikes have to be separated from real features. The criteria applied were chosen to agree with a visual inspection of the spectra. Features have to be stronger than 3 sigma in T_{on-off} to be identified. To determine the line of sight distance corresponding to a given radius interval we used the rotation curve from Brand and Blitz (1993). Mathematically for any radial bin

the feature density is given by,

$$\# \text{ features / kpc} = \frac{\sum_{sources} \# \text{ features / kpc}}{N_{bin}} \quad (9)$$

where N_{bin} is the total number of sources contributing to any given bin.

Figure 13 shows the density of features as a function of Galactocentric radius for two optical depth cut-off levels. The solid histogram is for all features with $\tau > 0.5$, while the dashed histogram is for $\tau > 1.5$. The error bars indicate the standard deviation in the bin divided by the square-root of the number of sources contributing to each bin. We show an exponential least-squares fit to the distribution for $\tau > 0.5$ which is given by $19.7e^{-0.36R}$ features/kpc, and which describes the distribution quite well. As the histogram for $\tau > 1.5$ illustrates, higher optical depth features are clearly concentrated in the local and Perseus arms and disappear entirely beyond 16 kpc. Garwood and Dickey (1989) found the feature density for all peak values of τ to have an average value of about $0.42 \pm 0.08 \text{ kpc}^{-1}$ from $R = 0$ to 4.25 kpc and 0.8 ± 0.1 from $R = 4.25$ kpc to 8.5 kpc which agrees with our results. The feature density thus seems to reach a peak around the solar neighbourhood and decreases both in the inner and outer Galaxy.

We have to keep in mind though that as the line of sight distance increases, a given change in velocity becomes a larger and larger change in line of sight distance due to the rotation curve. While 1.32 km/s (our spectral resolution) locally corresponds to about 200 to 300 pc (using the rotation curve to convert from velocity to distance), at -100 km/s the same velocity corresponds to scales from 200 pc to a few kpc (depending on longitude). Thus, if the dominant scale of structure in the H I is on the order of a 100 pc rather than several hundred parsecs to kiloparsecs, then this observed radial dependence could at least partially be an observational effect. As we look further and further away along the line of sight, we lose clouds in our identification due to the decreasing spatial resolution. In the outer Galaxy, an increase in the line of sight distance always corresponds to an increase in Galactocentric radius. Thus, since our data is largely in the outer Galaxy, the observed effect will give a drop in the number of features.

4. CONCLUSIONS

We have presented a new emission-absorption survey of the Galactic Plane at 21-cm with an unprecedented source density of about 0.6 sources per square degree. In agreement with previous studies we find spin temperatures between 40 K and 300 K. Due to the difficulty in interpreting the spin temperature we apply a simple 2-component model to the data. We

find T_c and $T_w\tau_w$ ranging from approximately 50 K to 80 K, and 0 K to 60 K respectively. Both T_c and $T_w\tau_w$ show a peak at about 14 kpc and a decrease in the outer Galaxy.

The derived density of neutral atomic hydrogen varies roughly as $e^{-0.3R}$, with Galactocentric radius (in kpc). However directly interpreting this as a drop in gas density with radius is complicated by the presence of the Galactic warp and the changing scale height visible in the z profile of N. Comparing the column density traced by emission to the total column we find that on average the emission traces about 75% of the total H I mass, and at the highest optical depths only about 65%.

We looked for evidence of very cold hydrogen in the Galaxy in our two-component model results and the spin temperature. This yielded a list of 5 features, with $T_s < 40$ K and lying below the two-component model lower envelope. Further a comparison to CO shows that even though there is no overall correlation between CO emission and H I absorption, about half the spectra show at least one H I absorption feature with clearly associated CO emission.

This study is a first look at the H I absorption in the CGPS. We hope to continue this analysis by incorporating the Southern and the VLA Galactic Plane Surveys (McClure-Griffiths et al. 2001; Taylor et al. 2003), giving us more information on the inner Galaxy, and the difference between the southern and northern parts of the Galactic plane. While the 2-component model applied here gives us some interesting results, it is clear that a more detailed feature by feature analysis could reveal much new information. This will also be pursued further.

We wish to thank J.M. Dickey, S.J. Gibson, and C. Heiles for helpful comments and discussions. Thanks also to J.C. Brown for her help with IDL and to L.A. Higgs for modifying the DRAO software for our purposes.

REFERENCES

- Brand, J., Blitz, L. 1993, A&A, 275, 67
- Braun, R., Walterbros, R.A.M. 1992, ApJ, 386, 120
- Clark, B.G. 1965, ApJ, 142, 1398
- Colgan, S.W.J., Salpeter, E.E., Terzian, Y. 1988, ApJ, 328, 275
- Dickey, J.M. 2002, in ASP Conf. Ser. 276, Seeing Through the Dust, ‘ ed. A.R. Taylor, T.L. Landecker & A.G. Willis (San Francisco:ASP), 248

- Dickey, J.M., Lockman, F.J. 1990, *ARA&A*, 28, 215
- Dickey, J.M., Kulkarni, S.R., van Gorkum, J.H., Heiles, C.E. 1983, *ApJS*, 53, 591
- Dickey, J.M., McClure-Griffiths, N.M., Gaensler, B.M., Green, A.J. 2003, *ApJ*, 585, 801
- Dickey, J.M., Mebold, U., Stanimirovic, S., Staveley-Smith, L. 2000, *ApJ*, 536, 756
- Dickey, J.M., Salpeter, E.E., Terzian, Y. 1978, *ApJS*, 36, 77
- Field, G.B., Goldsmith, D.W., Habing, H.J. 1969, *ApJ*, 155, L149
- Garwood, R.W., Dickey, J.M. 1989, *ApJ*, 338, 841
- Gibson, S.J., Taylor, A.R., Higgs, L.A., Dewdney, P.E. 2000, *ApJ*, 540, 851
- Heiles, C., Troland, T.H. 2003a, *ApJS*, 145, 329
- Heiles, C., Troland, T.H. 2003b, *ApJ*, 586, 1067
- Heyer, M.H., Brunt, C., Snell, R.L., Howe, J.E., Schloerb, F.P. Carpenter, J.M. 1998, *ApJS*, 115, 241
- Hughes, M.P., Thompson, A.R., Colvin, R.S. 1971, *ApJS*, 23, 323
- Kavars, D.W., Dickey, J.M., *ApJ*, accepted
- Knee, L.B.G., Brunt, C.M. 2001, *Nature*, 412, 308
- Kolpak, M.A., Jackson, J.M., Bania, T.M., Dickey, J.M. 2002, *ApJ*, 578, 868
- Kulkarni, S.R., Heiles, C. 1988, in *Galactic and Extragalactic Radio Astronomy*, Verschuur, ed. G.L., Kellermann, K.I., Berlin: Springer, 117
- Landecker, T.L., et al. 2000, *A&AS*, 145, 509
- Lazareff, B. 1975, *A&A*, 42, 25
- McKee, C.F., Ostricker, J.P. 1977, *ApJ*, 218, 148
- McClure-Griffiths, N.M., Green, A.J., Dickey, J.M., Gaensler, B.M., Haynes, R.F., Wieringa, M.H. 2001, *ApJ*, 551, 394
- Mebold, U., Winnberg, A., Kalberla, P.M.W., Goss, W.M. 1982, *A&A*, 115, 223
- Meyerdierks, H., Heithausen, A. 1996, *A&A*, 313, 929

- Payne, H.E., Salpeter, E.E., Terzian, Y. 1982, ApJS, 48, 199
- Radhakrishnan, V., Murray, J.D., Lockhart, P., Whittle, R.P.J. 1972, ApJS, 24, 15
- Reach, W. T., Koo, B., Heiles, C. 1994, ApJ, 429, 672
- Taylor, A.R. 1999, in ASP Conf. Ser. 168, New Perspectives on the Interstellar Medium, ed. A.R. Taylor, T.L. Landecker & G. Joncas (San Francisco:ASP), 3
- Taylor A.R., et al. 2003, AJ, 125, 3145
- Taylor, A.R., Stil, J.M., Dickey, J.M., McClure-Griffiths, N.M., Martin, P.G., Rothwell, T., Lockman, F.J. 2002, in ASP Conf. Ser. 276, Seeing Through the Dust, ed. A.R. Taylor, T.L. Landecker & A.G. Willis (San Francisco:ASP), 68

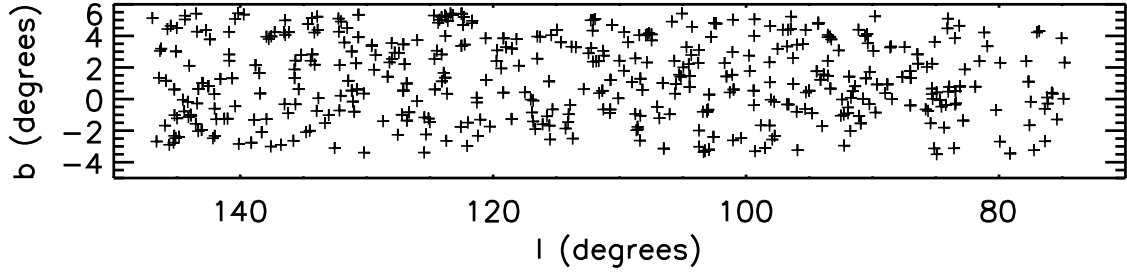


Fig. 1.— Location of sources used for this work.

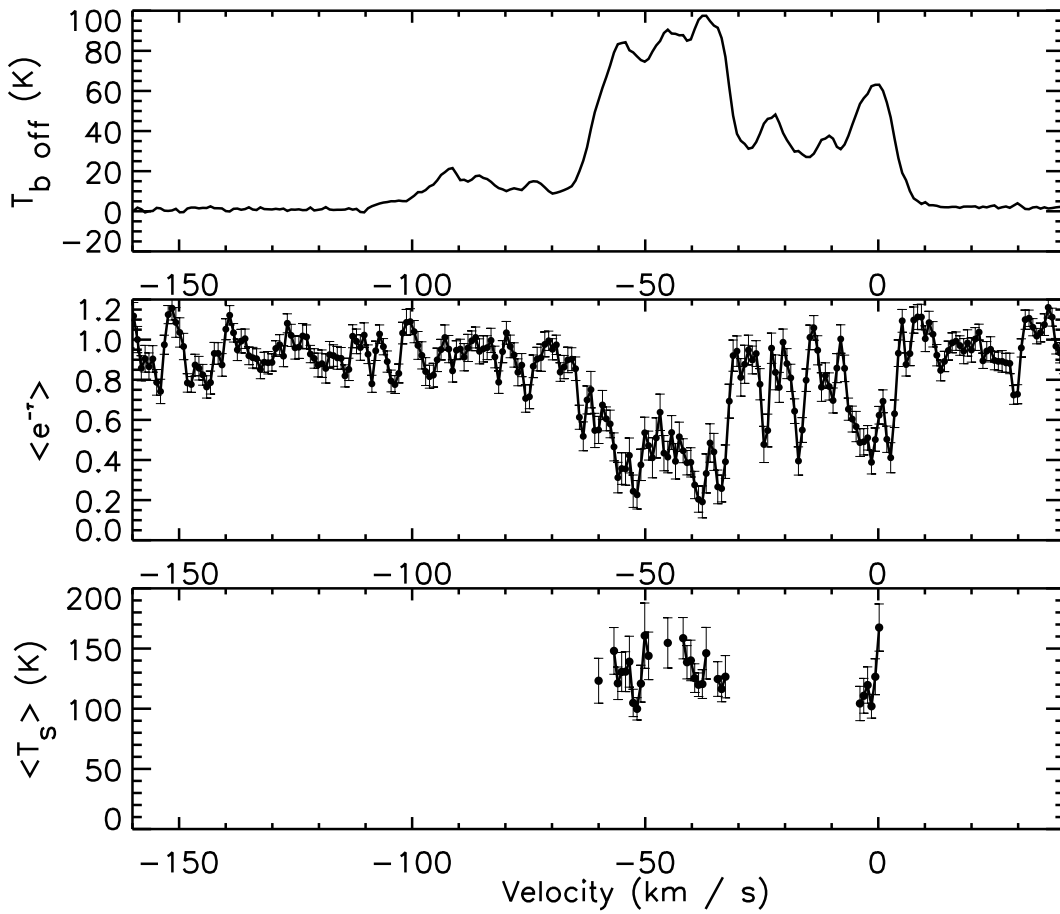


Fig. 2.— Spectra for Maffei 2 ($T_{bg} = 32 \text{ K}$). 1σ error bars are shown.

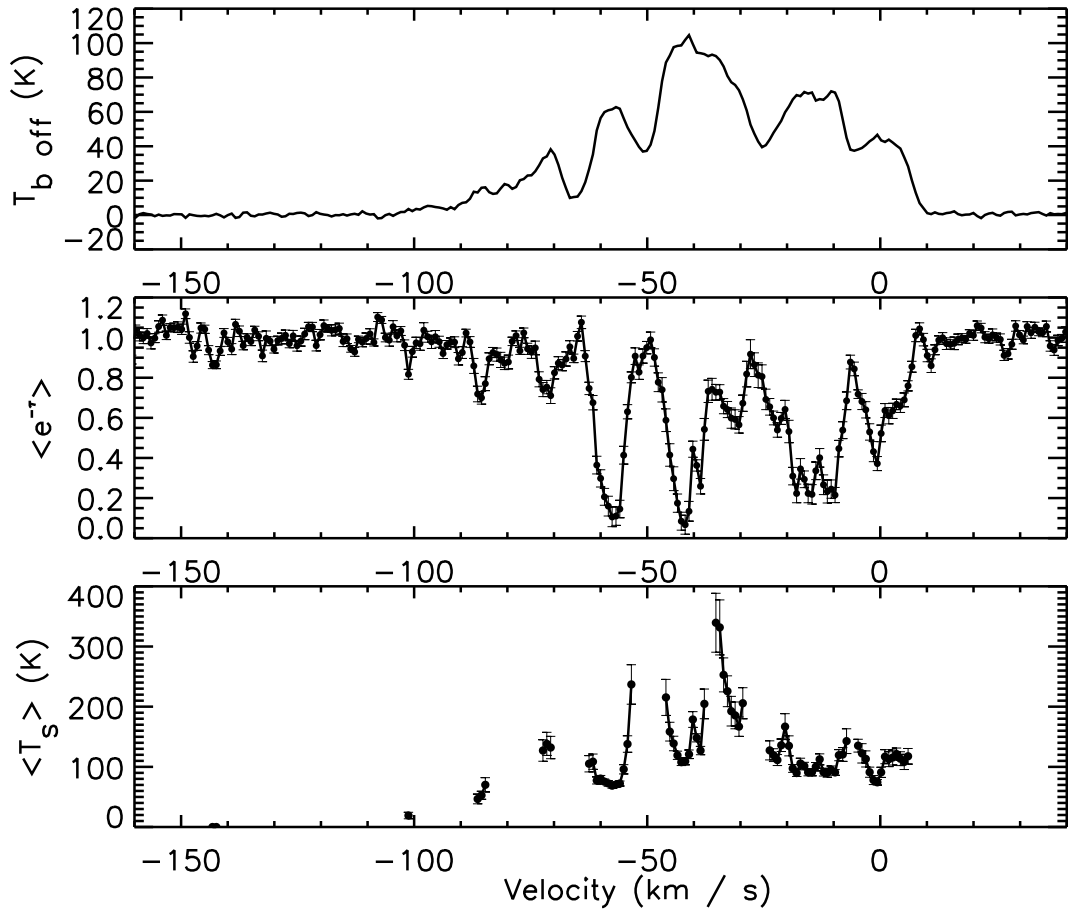


Fig. 3.— Spectra for 87GB 032246.6+572847 ($T_{bg} = 77$ K).

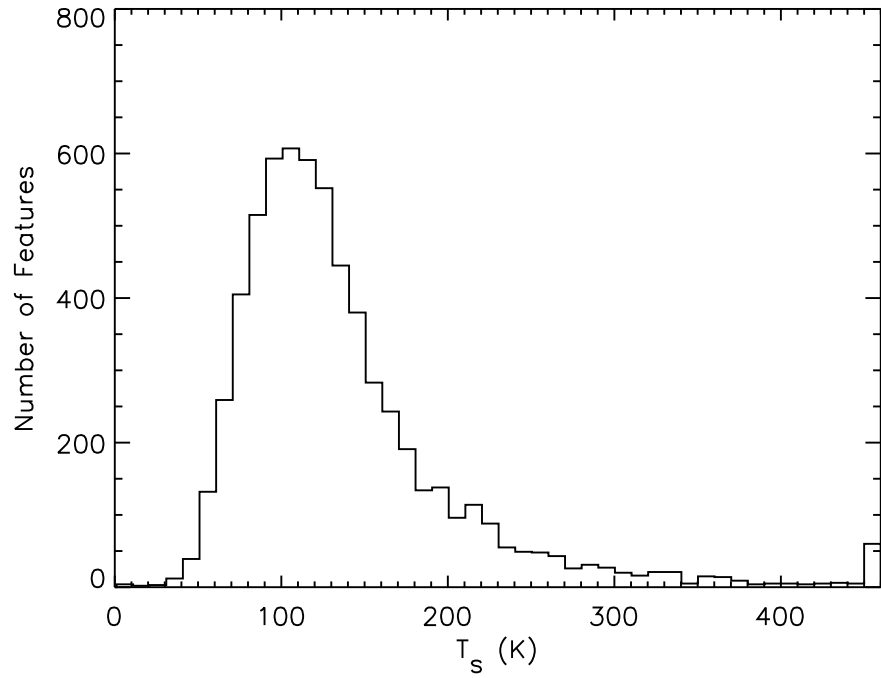


Fig. 4.— The distribution of spin temperatures for all channels where T_{on-off} S/N > 5. The last bin contains all channels with T_s higher than 450 K.

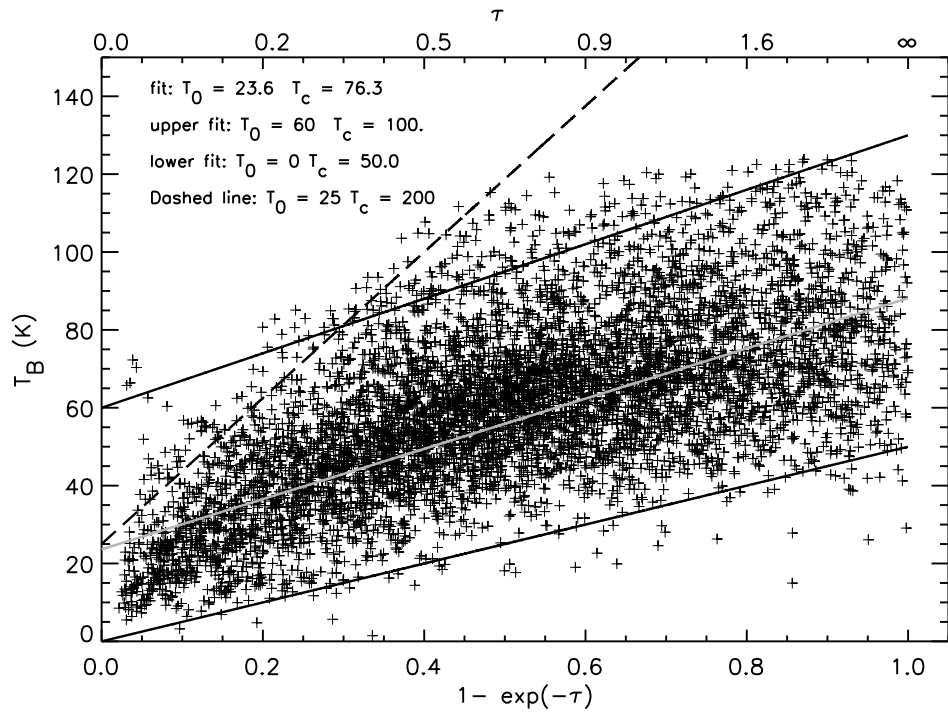


Fig. 5.— T_B versus $1 - e^{-\tau}$ with least squares fit and envelopes. The optical depth goes to zero on the left, and approaches infinity on the right.

Table 1. Cold Spin Temperature Features

Source Name	l (deg)	b (deg)	v (km/s)	T_s (K)	ΔT_s (K)	τ	T_B (K)	T_c (K)
4C+35.49	76.366	-2.674	-74.02	36	3	0.71	18	20
MG4 J203647+4654	85.089	3.620	-103.70	18	2	1.94	15	4
3C+434.1	94.112	1.223	-81.47	31	2	1.01	20	20
87GB 231107.2+625244	112.107	2.362	-93.80	27	2	3.00	26	19
87GB 020322.8+623159	131.459	1.157	-97.93	32	2	0.89	19	22

Note. — The values quoted are for the lowest T_s point in each feature. ΔT_s is the uncertainty in T_s .

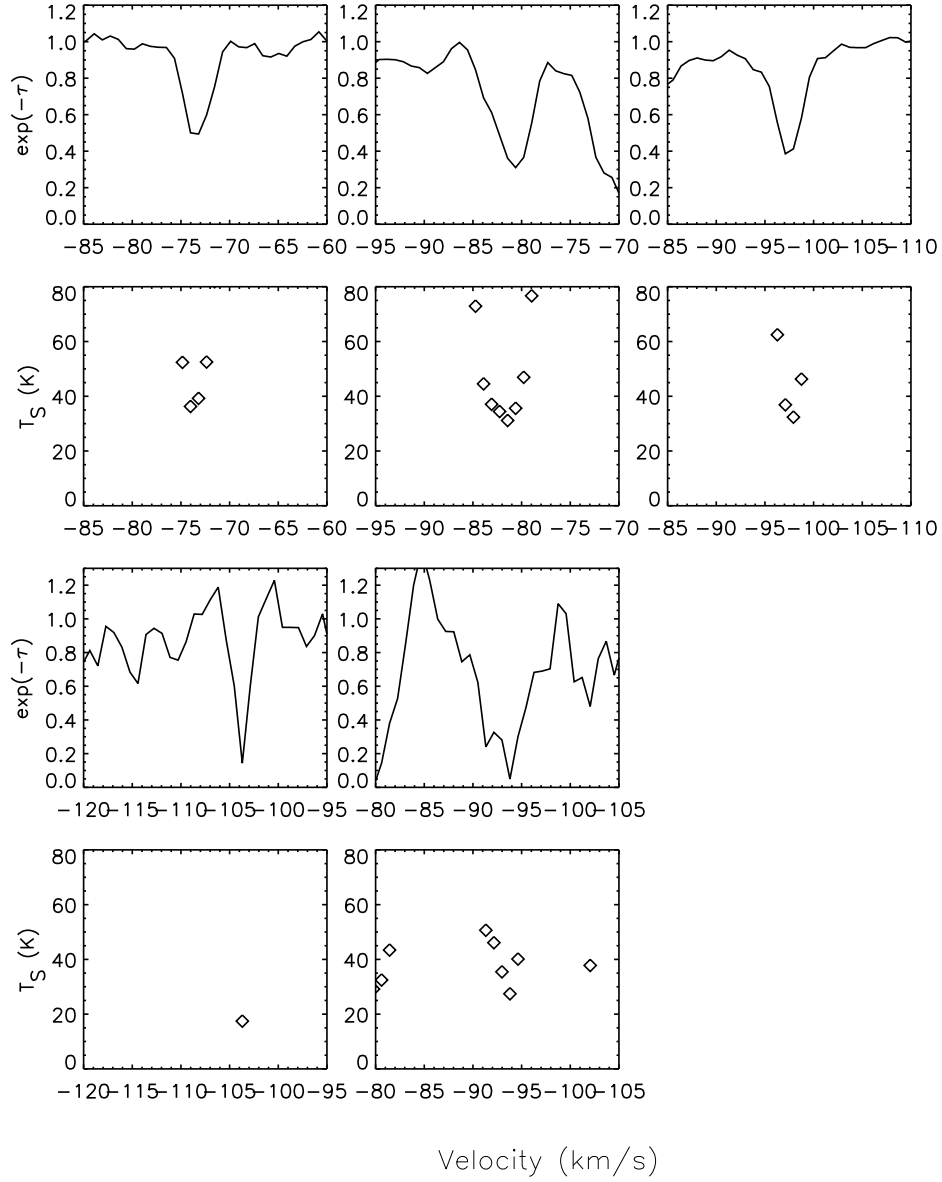


Fig. 6.— The optical depth and spin temperature line profiles for the 5 identified cold features. The arrangement from top left to bottom right is 4C +35.49, 3C 434.1, 87GB 020322.8+623159, MG4 J203647+4654, and 87GB 231107.2+625244.

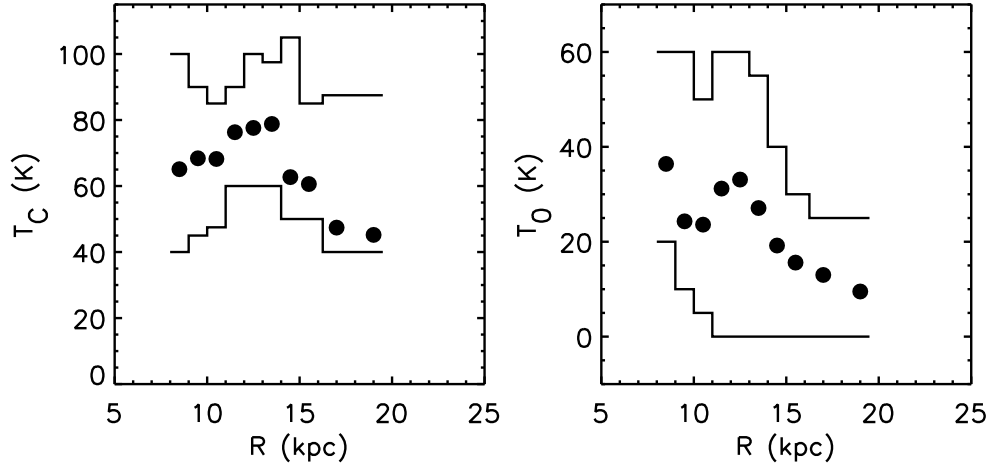


Fig. 7.— Radial variation of the cold component temperature (left) and $T_w \tau_w$ (right). The lines show the values of T_c and $T_w \tau_w$ derived from fitting the scatter envelopes. All values plotted are for $q = 0.5$.

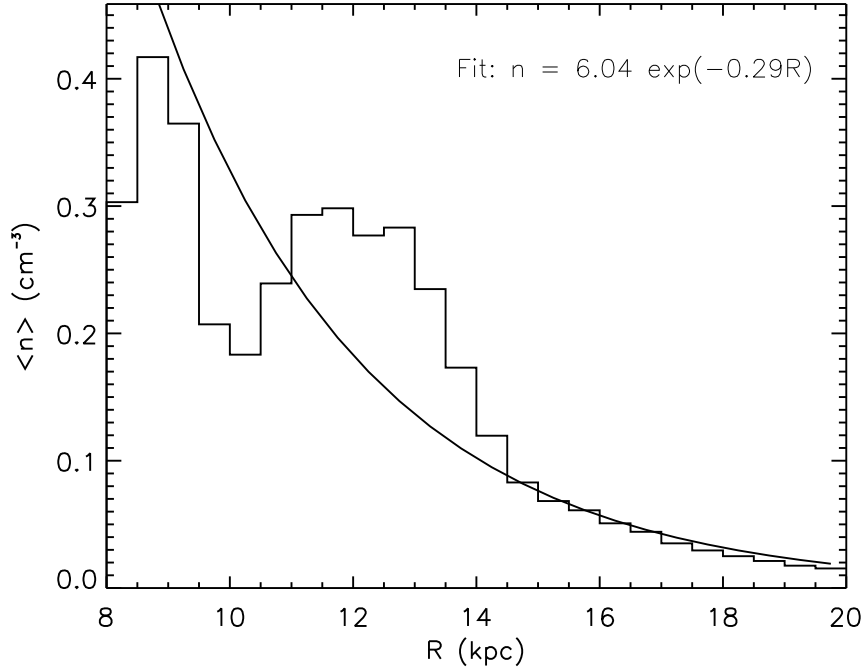


Fig. 8.— Mean spatial density versus Galactocentric radius. The distribution is least squares fit with an exponential function.

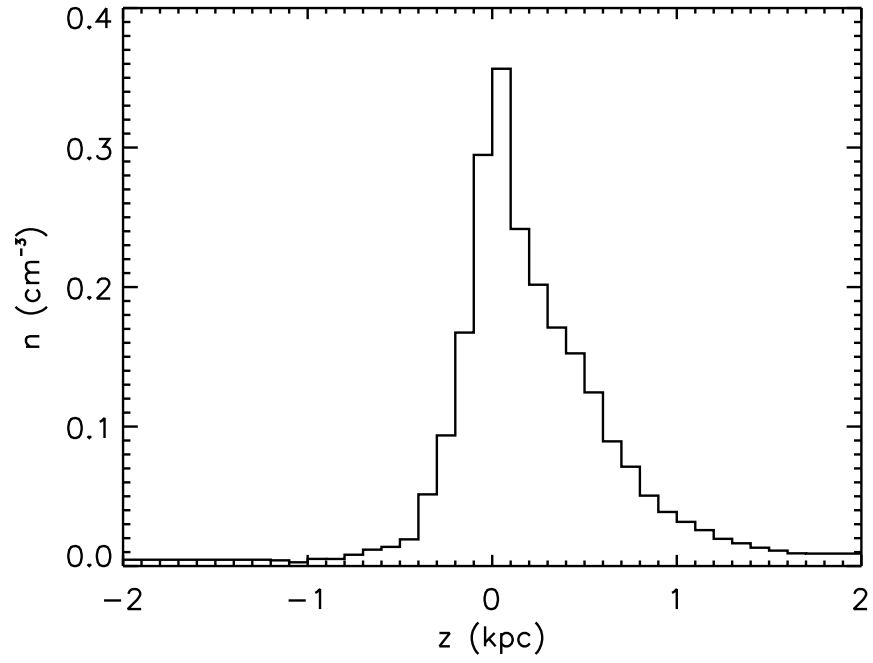


Fig. 9.— Mean spatial density versus height above the Galactic plane. Note that the “far” solution was used for channels where a velocity ambiguity exists (inside the solar circle).

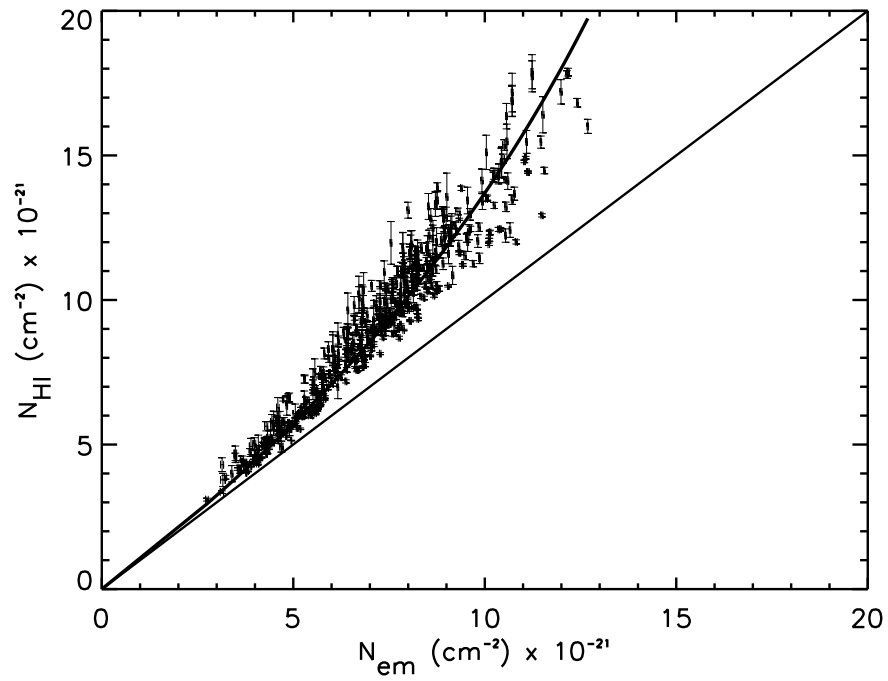


Fig. 10.— The emission column density versus total column density (assuming a one phase medium) for all the sources. The lines show a 1:1 relationship and an empirical fit to the data (equation 8).

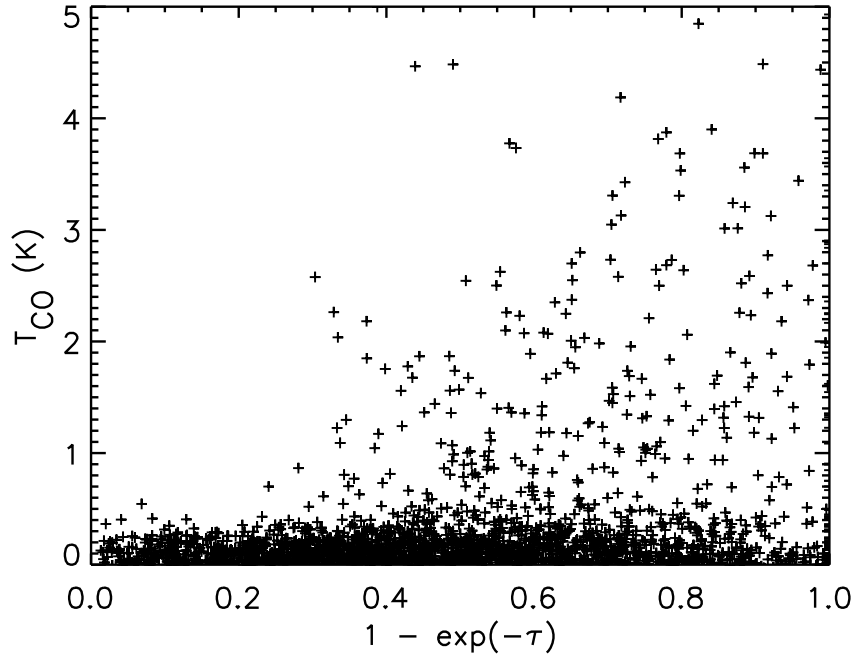


Fig. 11.— CO emission brightness temperature versus $1 - e^{-\tau}$ for the 134 sources that are in the FCRAO survey field.

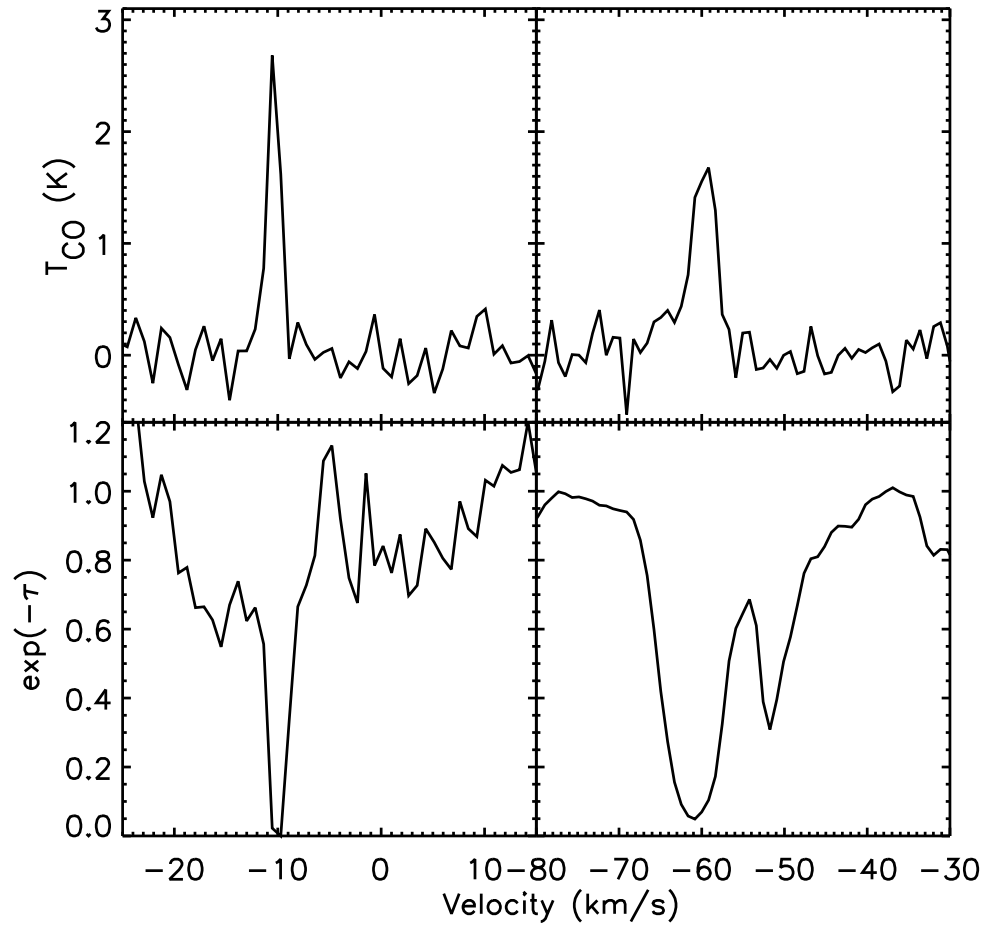


Fig. 12.— Two example features that appear both in CO and optical depth. On the left 87GB 013134.9+650922, on the right 3C 011.1.

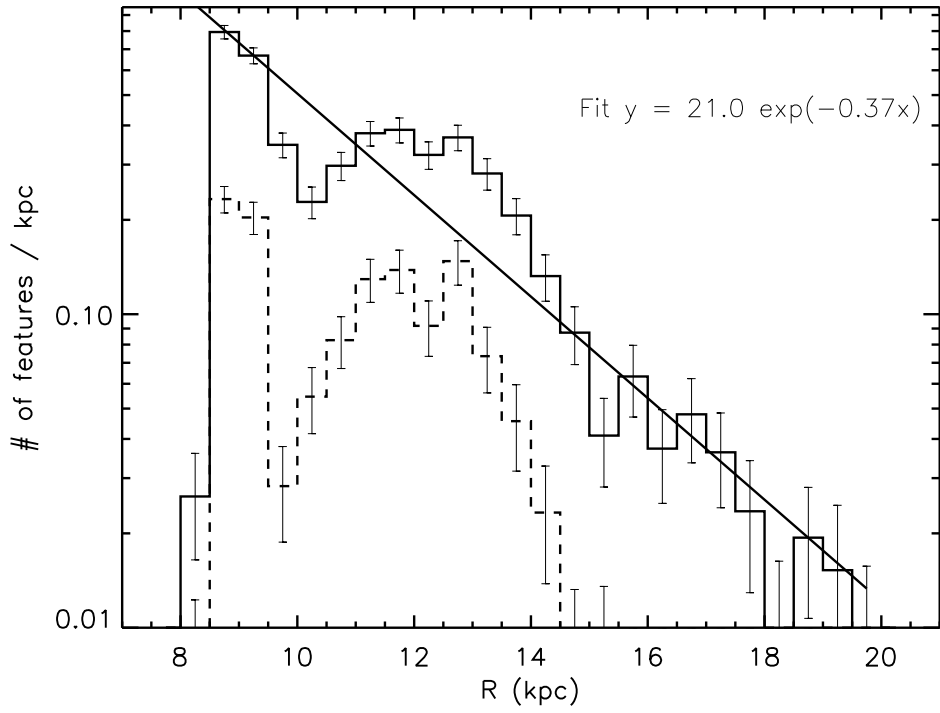


Fig. 13.— Feature density versus Galactocentric radius for features with peak $\tau > 0.5$ (solid) and $\tau > 1.5$ (dashed).